RESEARCH

Engineered (NH$_2$)-MIL-125(Ti)/copolymer@MnFe$_2$O$_4$ nanocomposite for synergistic eradication of cancer cells via DOX/pCRISPR delivery

Moein Safarkhani[1,2] · Amirhossein Ojaghi[2] · Shefa Mirani Nezhad[3] · Hossein Daneshgar[2] ·
Ana Cláudia Paiva-Santos[4,5] · Fatemeh Radmanesh[6,7] · Mojtaba Bagherzadeh[2] · Ehsan Nazarzadeh Zare[3] ·
Navid Rabiee[8,9] · Pooyan Makvandi[10,11]

Abstract

The present study proposed an innovative nanocomposite aimed at enhancing gene and drug delivery for cancer treatment. The nanocomposite was composed of amine-functionalized metal–organic frameworks, (NH$_2$)-MIL-125(Ti), conjugated to poly(aniline-*co*-para-phenylenediamine), and coated on manganese ferrite nanoparticles that were utilized to co-deliver the chemotherapy drug doxorubicin (DOX) and plasmid CRISPR (pCRISPR) to cancer cells. The investigation focused on whether surface modification with amine groups could improve cellular uptake and transfection efficiency. In addition, the study also utilized an engineered cell-imprinted substrate to mimic the cellular environment and enhance the delivery and expression of edited genes. The results demonstrated the proposed nanocarriers successfully co-delivered DOX and pCRISPR, indicating their potential for combination cancer therapy. Specific highlights include (1) reliable platform for multi-drug delivery based on the (NH$_2$)-MIL-125(Ti)/poly(aniline-*co*-para-phenylenediamine)/MnFe$_2$O$_4$ nanocomposite structure; (2) hemocompatibility analysis revealed less than 1% hemolysis, pointing to biosafety; (3) amine surface modification enhanced cellular uptake up to 38.3% in A549 cells, improving transfection; (4) the cell-imprinted substrate enhanced therapeutic efficacy by promoting delivery and expression in a physiologically relevant microenvironment. Overall, this study makes significant contributions to gene delivery and expression for cancer therapy. The engineered nanocomposite, amine surface modification, and cell-mimetic substrate employ innovative strategies to augment the efficacy of combination gene and drug therapy against cancer.

Keywords MIL-125(Ti) · Imprinted cell culture · Gene/drug delivery · Copolymer · Manganese ferrite · Nanocomposite

1 Introduction

Metal–organic frameworks (MOFs) have emerged as a promising class of materials with unique properties and structures, which make them highly attractive for various biomedical applications [1–3]. MOFs are a type of porous material constructed from metal ions or clusters that are linked together by organic ligands [4, 5]. They offer a range of tunable properties, including high surface area, uniform pore size distribution, and tailorable chemical and physical properties [6–9], which make them highly versatile for use in drug delivery, sensing, and imaging applications [10]. However, the critical special factors that make MOFs highly desirable for biomedical applications are their potential to be modified with significant biocompatibility and biodegradability

[11, 12]. MOFs decorated with polymers and natural components are non-toxic and non-immunogenic, making them an excellent choice for use in drug delivery systems [13, 14]. Additionally, they can be designed to degrade under physiological conditions, making them an ideal candidate for targeted drug delivery and bioimaging applications [15]. Zheng et al. incorporated polycaprolactone copper-based MOF by hydrogen bonding and they reported that their design led to gradual degradation and release of copper ions which promoted cell proliferation [16]. MOFs also offer the advantage of being able to carry a large payload of drugs or imaging agents due to their high porosity and large surface area, providing improved efficacy and reduced toxicity compared to conventional drug delivery systems [17]. Molavi et al. reported robust water-stable UiO-66-derived MOFs with the highest adsorption ability of 423.85 mg/g and 540.78 mg/g for curcumin and methotrexate respectively [18].

Furthermore, the MOFs' unique structural and functional properties can be engineered to specifically target and bind to biological molecules, enabling them to be used as highly sensitive biosensors and imaging agents for early disease detection and diagnosis [19, 20]. In recent years, there has been growing interest in the development of nanocomposites for various applications due to their unique physicochemical properties [21, 22]. However, the inherent properties of these nanomaterials may not always meet the specific requirements of a particular application, such as biocompatibility, stability, or solubility [23]. This has led to a growing interest in surface decoration with polymers as a means of modifying and enhancing the properties of these inorganic nanomaterials. The performance and properties of MOF/polymer composites depend on their interactions like encapsulation, metal-polymer coordination, and covalent and non-covalent attachment [24].

Surface decoration with polymers involves the attachment of polymeric chains onto the surface of inorganic nanomaterials to improve their performance or to impart specific functionalities [25]. The polymers can be grafted onto the surface of the nanomaterials through covalent bonding, electrostatic interactions, or physical adsorption. Liu et al. screened non-covalent surface modification of iron-based MOF (NH_2-MIL-101(Fe)) by MOF's surface positive charge. They found that their design led to considerable stability [26, 27]. The use of polymers for surface decoration of inorganic nanomaterials can lead to a variety of improvements in their characteristics. For example, the attachment of hydrophilic polymers can increase the solubility and stability of nanomaterials in aqueous solutions, which is important for biomedical applications [28, 29]. Polymers can also be used to improve the biocompatibility of nanomaterials by reducing their toxicity and immunogenicity [30]. Fan and coworkers investigated the polymer-based coating effect on decreasing immunogenicity. They reported that utilizing PEGylated beta-cyclodextrin polyethyleneimine has altered the biodistribution and reduced the immunogenicity [31]. In addition, polymers can be used to impart specific functionalities to nanomaterials, such as targeting specific cells or tissues in the body for drug delivery applications. For example, polysaccharide-based coated systems revealed remarkable applicability in colon cancer-targeted delivery [32]. There are several ways to achieve surface decoration of inorganic nanomaterials with polymers [33]. One approach involves the use of block copolymers, which have both hydrophilic and hydrophobic segments, to form a layer of polymer chains on the surface of the nanomaterials. Another approach involves the use of cross-linking agents to covalently attach polymers to the surface of the nanomaterials. Additionally, electrostatic interactions can be used to attach charged polymers to the surface of oppositely charged nanomaterials. Last but not least, the incorporation of conductive polymers facilitates internalization and endosomal escape within cancer cells due to high charge density, boosting transfection efficiency. Additionally, their electrical properties allow triggered drug release upon near infrared or photothermal irradiation [34].

The development of co-delivery systems for therapeutic applications has gained significant interest in recent years due to their potential to enhance therapeutic efficacy and reduce toxicity [35, 36]. The profitable enhancement and development of co-delivery systems necessitate an all-embracing comprehension of the fundamental physicochemical features and interactions inherent in involved compounds. Synthesizing a single compound that satisfies all requirements is implicitly complicated. One of the most promising approaches for taking advantage of various components' features simultaneously is an amalgamation of them to achieve nanocomposites. Through the composition of various compounds and optimizing their weight ratio, the final composites will reveal all desirable features without demonstrating nuisance characteristics. This is where merging fundamental and advanced studies can play a critical role in improving the performance of co-delivery systems. Another area of interest in co-delivery systems is the functionalization of noncompounds. As a promising functional group, amine functionalization can improve the solubility and stability of nanoparticles in biological fluids and enhance their cellular uptake [37, 38]. Gong and colleagues have studied amine-functionalized silica nanoparticles for the simultaneous delivery of candesartan and angiostatin plasmid for breast cancer therapy. They reported that although the silica-based amine-functionalized nanoparticles did not reveal cytotoxicity, the loaded nanocarrier demonstrated considerable efficiency and gene transfection [39]. However, the impact of amine functionalization on the performance of co-delivery systems is not fully understood and they are still at the beginning of the path.

Another area of interest in co-delivery systems is the use of MOFs and magnetic nanoparticles. MOFs unique properties make them attractive for co-delivery applications. Magnetic nanoparticles can be used for targeted delivery, enhanced cellular uptake, as a contrast agent in magnetic resonance imaging, and as a chemodynamic therapy agent [40]. As a scientific and proven fact, the concentration of H_2O_2 in the tumor microenvironment is high, and based on the Fenton mechanism, the interaction between H_2O_2 and magnetic nanoparticles leads to ROS (reactive oxygen species) generation which chemo-dynamically eradicates the cancerous cells. $MnFe_2O_4$ (a multifunctional spinel ferrite) has been reported as a highly efficient catalyst in a heterogeneous Fenton-like reaction owing to the transformations among metal ions with inconstant valence states [41–43]. The most important feature of magnetic nanoparticles is the hyperthermia treatment ability that leads to tumorous

cells' fast killing which can be activated in the magnetic field [44–46]. Nha et al. conducted a study in which they investigated the temperature-increasing ability of $MnFe_2O_4$ to contain nanoparticles. Based on their report, their engineered dual hyperthermia agent demonstrated a 2.7 times more specific absorption rate (0.14 W cm^{-2} laser and 100 Oe magnetic field) in comparison with only magnetic field. The most interesting part of their report is that the synergistic effect of photo- and magneto-thermal characteristics of fabricated nanoparticles could reduce the required laser intensity and irradiation time as well as decrease the magnetic field strength [47]. Also, Hemmat et al. conducted a study on reducing mucociliary clearance of magnetic-based drug delivery systems. They found that their fabricated compound revealed significant improvement in vivo efficacy by implementing a magnetic field (on the glabellar region) in comparison with control groups [48].

Fundamental studies can provide insights into the interactions between MOFs, magnetic nanoparticles, and amine-functionalized nanoparticles with biological systems, while advanced studies can explore the optimization of co-delivery systems that incorporate these components based on these fundamental insights. The combination of fundamental and advanced studies can lead to significant improvements in the performance of co-delivery systems. By understanding the physicochemical properties and interactions of different components, researchers can optimize the design and formulation of co-delivery systems for specific applications. This approach can lead to more effective and efficient therapies that can improve patient outcomes. Regarding, the present work presents an innovative approach to enhance gene delivery and expression in cancer cells. The study utilizes nanostructures composed of MIL-125(Ti) conjugated poly(aniline-*co*-para-phenylenediamine)@manganese ferrite to co-deliver doxorubicin (DOX) and pCRISPR, to cancer cells. We sought to illustrate how nanostructure surface modification with amines enhances their uptake by cells, thereby boosting the transfection efficacy. In addition, by preparation of a substrate, we tried to mimic the cellular environment conditions. Notably, this study did not focus on optimizing the size.

2 Materials and methods

Aniline (Merck) was purified by double distillation. Para-phenylenediamine (*p*PDA) and ammonium persulfate (APS), manganese chloride tetrahydrate, ferric chloride hexa hydrated, and sodium hydroxide were purchased from Merck Company. All solvents and reagents were purchased from Merck and Sigma-Aldrich (Germany) and used freshly. FT-IR (Unicam Maston 1000, KBr pellet), UV–Vis (Carrying 100 BioVarian, 10 mm path length), FESEM and EDS

(MIRA3 TESCAN), 2D fluorescence image: (FACSCalibur (BD, Germany)) and (Olympus-BX51), PXRD (PANalytical company X'Pert Pro MPD), zeta potential, and DLS (HORIBA SZ-100) were employed for the chemical characterization of the products. The Specific Surface Analyzer II (Micromeritics, 3Flex) has been utilized for BET analysis and the JEM2100F/JEOL has been used for FE-TEM imaging.

2.1 Fabrication of poly (aniline-*co*-para phenylenediamine)@MnFe$_2$O$_4$ nanocomposite (PA*p*PDA@MnFe$_2$O$_4$) (C2)

PA*p*PDA@MnFe$_2$O$_4$ nanocomposite was fabricated by in situ copolymerization method as follows (Scheme 1A): In a 250-mL flask, an equal molar ratio of Ani (Aniline) and *p*PDA (para-phenylenediamine) monomers were dissolved in 100 mL of HCl solution (0.1M) at room temperature with a magnetic stirrer; then, 20 mL dispersed MnFe$_2$O$_4$ nanoparticles (10 wt% to monomers) were added to the previous solution. The solution was degassed by an inert gas for 30 min. Copolymerization was initiated upon adding 25 mL of the APS (ammonium persulfate) solution (1 M) for 15 min. The reaction mixture was kept under continuous agitation using a magnetic stirrer under an N$_2$ atmosphere for 24 h. In the end, the precipitated nanocomposite was separated by an external magnet and washed several times with distilled water and methanol. Finally, the resulting powder was dried in a vacuum oven at 60 °C for 24 h. Poly(para-phenylenediamine)@MnFe$_2$O$_4$ (P*p*PDA@MnFe$_2$O$_4$) (C1) nanocomposite was also fabricated according to the above method whereas only used para-phenylenediamine monomer. All characterization analyses (FT-IR, XRD, FESEM/EDX, TGA, and VSM) of poly(para-phenylenediamine), poly(aniline-*co*-para-phenylenediamine), poly(para-phenylenediamine)@MnFe$_2$O$_4$, and poly (aniline-*co*-para-phenylenediamine)@MnFe$_2$O$_4$ nanocomposite are shown in the Supplementary materials (Figs. S1, S3, S4, S5, S8, S10, and S11).

2.2 Synthesis of manganese ferrite (MnFe$_2$O$_4$)

Magnetic manganese ferrite (MnFe$_2$O$_4$) was synthesized by in situ co-precipitation technique as follows (Scheme 1B): First, manganese chloride tetrahydrate and ferric chloride hexa hydrated salts with a molar ratio of 1:2 were dissolved in 100 mL of distilled water. Then, the above solution was added drop by drop to the sodium hydroxide solution (10 mL, 10%) to pH reached 10. Finally, the dark brown precipitate was formed and separated by a magnet and washed with distilled water until the pH of the residual solution reached 7. The obtained precipitate was then dried in an oven at 60 °C for 4 h and calcinated at 500 °C for 8 h to obtain the MnFe$_2$O$_4$. All catheterization analyses (FT-IR, XRD,
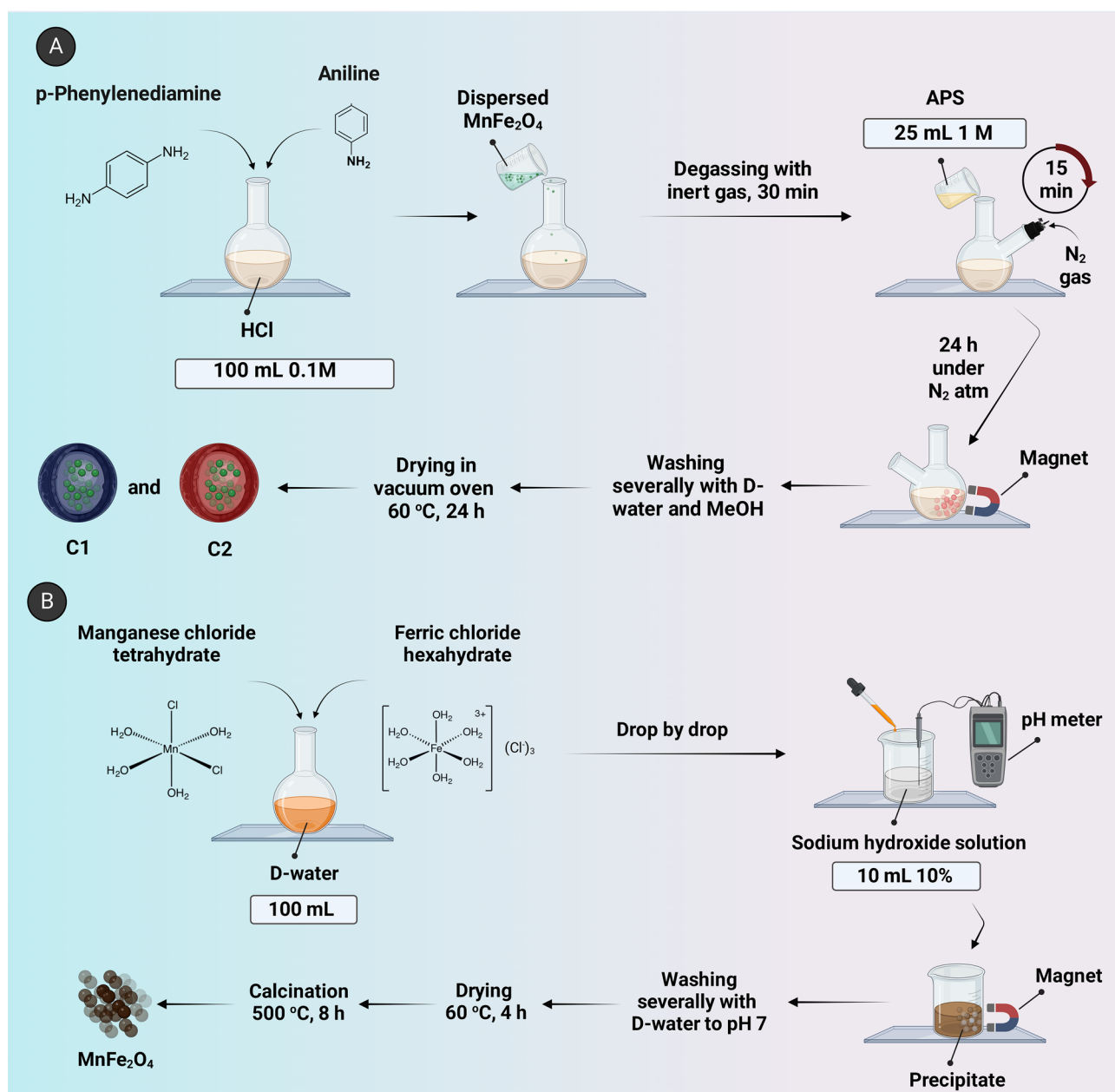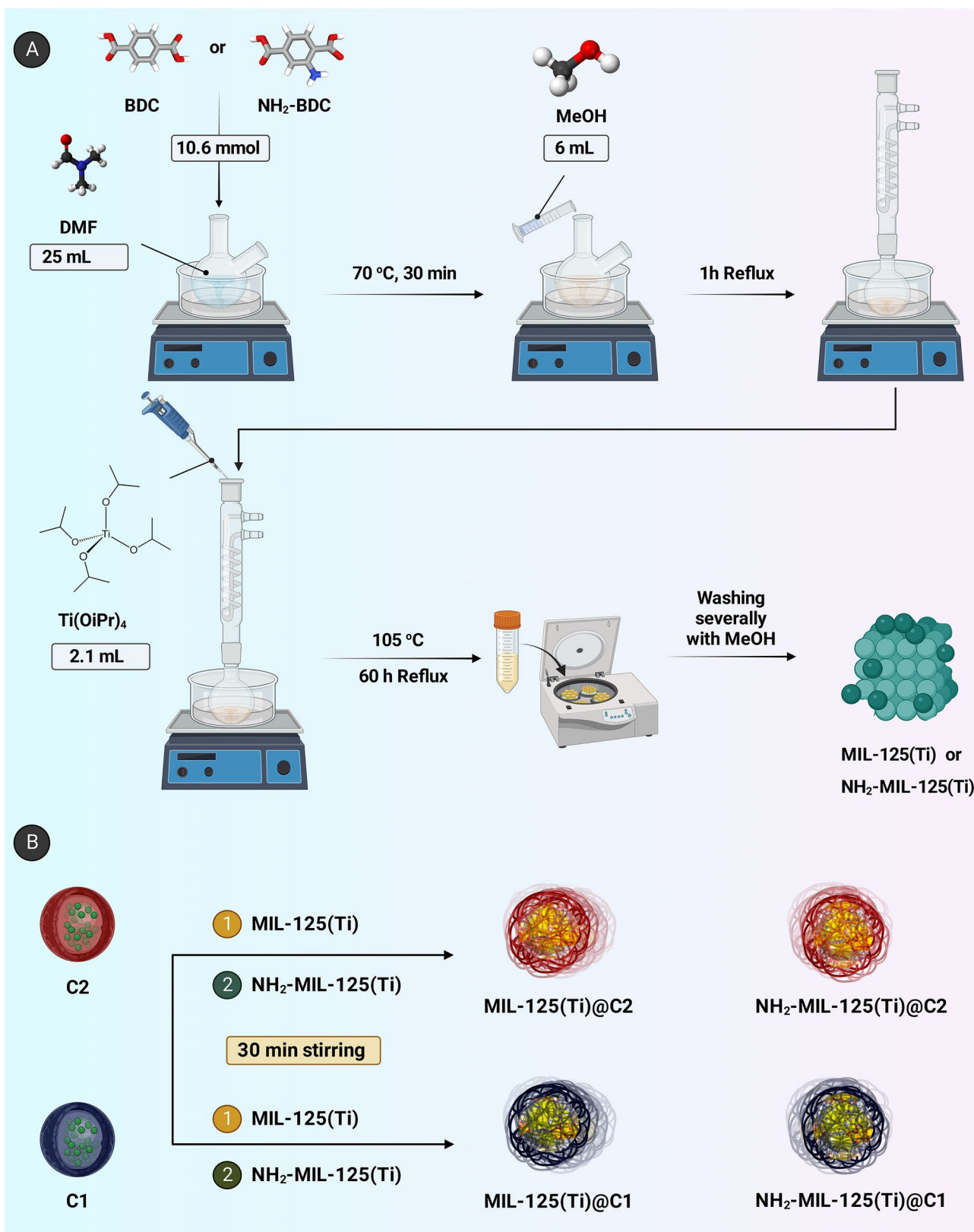
Scheme 1 The graphical synthesis procedure of **A** composites (C1 and C2) and **B** MnFe$_2$O$_4$

FESEM/EDX, TGA, and VSM) of MnFe$_2$O$_4$ are shown in the Supplementary materials.

2.3 Synthesis of MIL-125(Ti) and NH$_2$-MIL-125(Ti)

Different methods have been reported for the synthesis of MIL-125(Ti). Many procedures have been carried out using reflux or solvothermal conditions [49, 50]. Here, the reflux was chosen, which was optimized based on the previous report [51]. Briefly, 10.6 mmol BDC (Benzene-1,4-dicarboxylic acid) was added as a linker to 25 mL

DMF (N,N-Dimethylformamide) in a 250 mL round bottom flask (Scheme 2A). After 30 min of stirring in a 70 °C oil bath, 6 mL of methanol was added to the solution. The solution was refluxed for 1 h at a temperature of 95 °C. Next, 2.1 mL Ti(iPrO)$_4$ was added to the solution at a temperature of 105 °C, and the mixture was refluxed for 60 h. In the end, the contents of the balloon were separated using a centrifuge at 8000 rpm for 10 min, and the product was washed 3 times with methanol to reduce impurities. The synthesis of NH$_2$-MIL-125(Ti) was also done in the same way, with the difference in the step of adding the linker (NH$_2$-BDC).

Scheme 2 The graphical synthesis procedure of **A** MILs and **B** final compounds

2.4 Fabrication of final composites

The C1 and C2 nanocomposites have been loaded into and immobilized on the surface of MILs by 30 min stirring at room temperature in DI-water (Scheme 2B).

2.5 Drug (DOX) loading

The combination of DOX and nanocarriers was incubated separately (24 h, 4 °C) to obtain the DOX-loaded nanocomposites. They stirred at three different ratios (1:1, 1:2, and 2:1), and after 12 h, the centrifuge (7500 rpm, 10 min) was conducted for precipitation of DOX associated with nanocomposites. The nanocomposites' drug-loading efficiency has been determined by UV–Vis spectroscopy.

2.6 pCRISPR decorating on the surface of non-viral vectors

In the present study, a precise amount of every nanocomposite (38.5 mg/mL) has been blended with various weight ratios of pCRISPR (at RT and darkness) and optimized based on their results. The same condition as the MTT assay method has been deployed for the last mixture for 30 min. The self-assembly method was successfully conducted for pCRISPR decorating on the surface of the nanocomposite and described in our previous article [52].

2.7 MTT assay

The biocompatibility and relative cell viability of prepared nanocomposites have been evaluated by 3-(4,5-dimethylthiazol-2-yl)-2,5-diphenyltetrazolium bromide (MTT) assay. Three different types of cell lines of MCF-7 (ATCC HTB-22), HEK-293 (ATCC CRL-1573), and NIH3T3 (ATCC, CRL-6361) were used for the MTT assay. The nanocomposite-free medium was the control group, and for each experiment. The optical absorption of wells is read utilizing a microplate reader. Briefly, 1×10^4 cells/well were incubated (96 well plates), and after 24 h, the media was replaced with serially diluted compounds with various concentrations (300 μL, 1–50 mg/mL) and incubated for 24 and 48 h.

2.8 Cell imprinting

For improving the drug/gene-loaded nanocomposites' internalization to the cells, decreasing the nanocomposites concentration, and increasing the efficiency of site-specific drug/gene delivery, the cell-imprinted method is utilized. This technique is optimized based on the fabrication of Schwann cell-imprinted substrate. The method adopted from the previous reports by Bonakdar et al. [53, 54], and the PDMS kits consist of curing agents, and PDMS (1:1 ratio)

are used in this study. Briefly, the cured PDMS dropwise has been added to the fixed cells and incubated for a day at 37 °C. Due to removing the surface of the substrate from cells or proteins, the cured substrate was washed several with 1M NaOH and sterilized with UV irradiation for 30 min.

2.9 In vitro gene expression

The gene expression (in vitro) was completed, similar to our previously published article [55]. The experiments of transfection have been performed utilizing pCRISPR and the A549 cell line the GFP (Green Fluorescent Protein) has been expressed as a receptor. The transfection procedure has been done using prepared nanocomposites with various WR (weight ratio) to pCRISPR. The standard density of cells (1×10^4 cells per well) was seeded in the 96 well plates and incubated for 24 h in medium (300 μL), 5% CO_2 atmosphere, and 37 °C. The PBS (Phosphate-Buffered Saline) was used for rinsing the cells after reaching 60% confluence and then incubated for 4 h and at 37 °C with dispersed nanocomposites (100 μL) and culture medium (200 μL). The pCRISPR amount has been kept in each well at 1 μg. Medium-contained nanocomposites were replaced with FBS (Fetal Bovine Serum, 10%) and DMEM/F12 (Dulbecco's Modified Eagle Medium/F12), and before analysis of transfection efficacy, the cells were kept again for 24 h at 37 °C. In the last step, the fluorescence microscope was used to evaluate the transfection efficacy with GFP expression. The ImageJ 1.45 software was utilized for quantifying the GFP-positive cell surface (license: National Institutes of Health (USA)). The experiments have been done in triplicate.

2.10 Hemolysis assay

The hemocompatibility of prepared materials and fabricated composites was screened utilizing the hemolysis assay based on the previously published method with slight modification [56]. Briefly, collected blood from Wistar rats (female, 7 weeks old) in an EDTA (ethylenediaminetetraacetate) supplemented tube. Erythrocytes were collected and severally washed with PBS by 1200 *g* centrifugation (10 min). In the next step, erythrocytes were dispersed in PBS at 5% (v/v), and 75 μL was added to every well of a 96-well plate. Then, 150 μL of composites with various concentrations (1, 10, 50, and 100 μg/mL) were added to erythrocytes followed by gentle mixing and incubation for 30 min. Afterward, 400 *g* centrifugation was applied for 4 min, and 75 μL of supernatants was transferred to the new plate. At the last step using a plate reader (550 nm wavelength), the hemolytic activity was measured (BioTek Instruments; Winooski, VT, USA). 0.1% Triton-X and PBS (Sigma-Aldrich) have been utilized as positive and

negative controls, respectively. Experiments were repeated three times.

3 Results and discussion

3.1 Characterization

The synthesized loaded nanocomposites were characterized, and the results are reported as follows: XRD patterns revealed that MIL-125(Ti) had conjugated with C1 and C2 based on its characteristic diffraction peaks at $2\theta = 6.775°$, $9.734°$, and $11.664°$ for MIL-125(Ti)@C2, and $2\theta = 6.816°$, $9.759°$, and $11.675°$ for MIL-125(Ti)@C1 which are similar to MIL-125(Ti). In addition, NH$_2$-MIL-125(Ti) patterns showed similar results, characteristic diffraction peaks at $2\theta = 6.809°$, $9.771°$, and $11.676°$ for NH$_2$-MIL-125(Ti)@C2, and $2\theta = 6.824°$, $9.789°$, and $11.677°$ for NH$_2$-MIL-125(Ti)@C1 are close to the patterns of NH$_2$-MIL-125(Ti). The mentioned 2θ angles are related to (101), (200), and (211) crystallographic planes, respectively. These data proved that conjugation with C1 and C2 preserved the structure of MIL-125(Ti) and NH$_2$-MIL-125(Ti), and no degradation occurred in MIL-125(Ti) and NH$_2$-MIL-125(Ti) [57] (Fig. 1A). In another study, NH$_2$-UiO-66 was coated by p(HEMA) and p(NIPAM). Although the main pattern was repeated in XRD patterns of all coated compounds, the coating agents led to changes in the intensities and slight shifts of NH$_2$-UiO-66 XRD peaks [13]. It is noticeable that all other prepared compounds' XRD patterns are discussed in the supplementary (Figs. S8 and S9).

In the FT-IR spectra of the MIL-125(Ti)@C2 and MIL-125(Ti)@C1, the characteristic broad peak appeared around 3470 cm^{-1}, corresponding to the stretching vibrations of N–H bonds in polymers and O–H groups of water
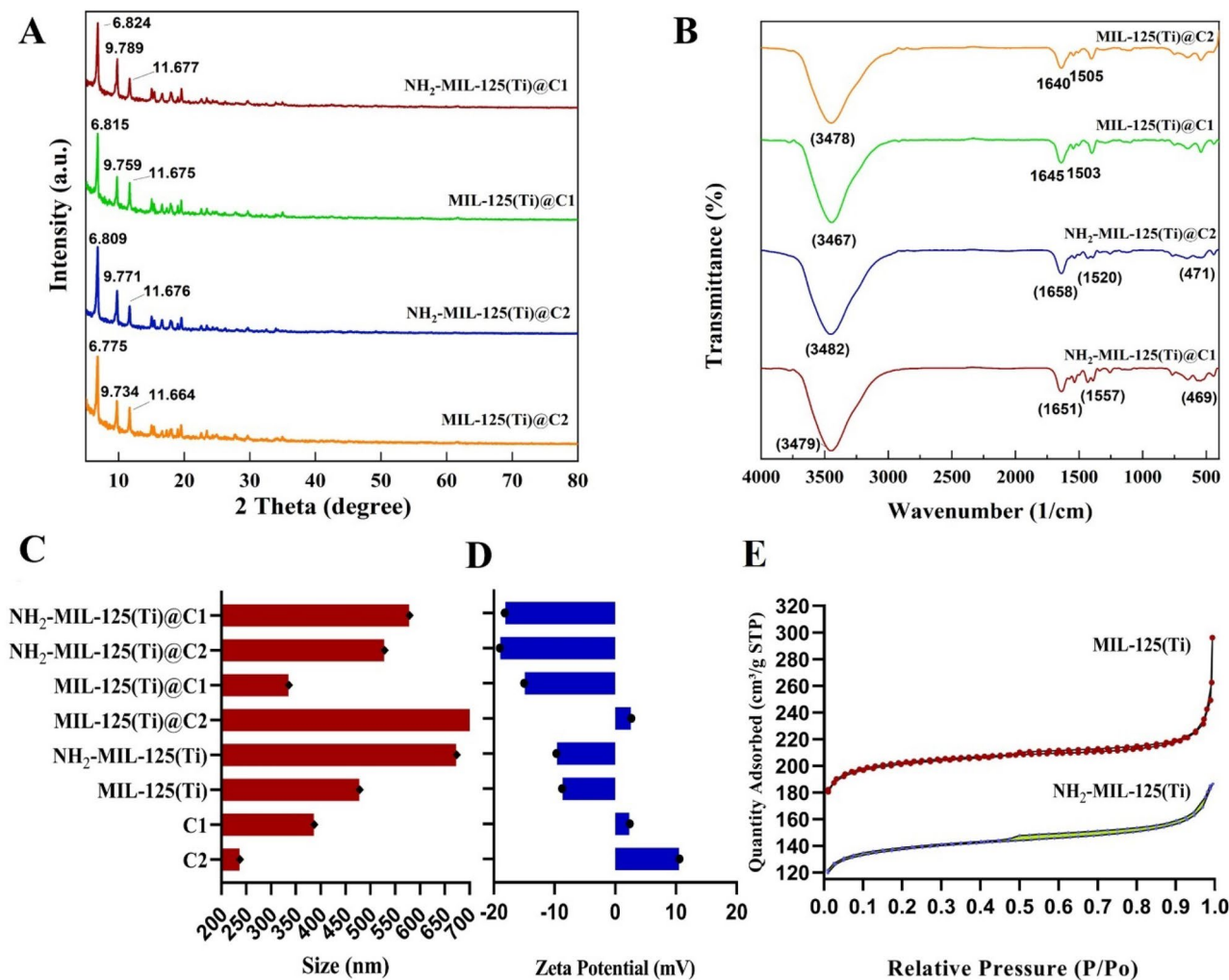

Fig. 1 **A** The XRD patterns, **B** FT-IR spectra, **C** DLS (Z-Average (r.nm)), **D** Zeta potential, and **E** Isotherm linear plot of compounds

solvent. The characteristic peaks that appeared around 1640 cm^{-1} and 1500 cm^{-1} are related to the stretching modes of quinoid imine and benzenoid amine units of C1 and C2, respectively. FT-IR spectra of NH_2-MIL-125(Ti)@ C2 and NH_2-MIL-125(Ti)@C1 demonstrated similar peaks; however, the presence of the amine group in the structure of NH_2-MIL-125(Ti) has increased the intensity of stretching and bending peaks of N–H groups. Symmetric stretching of C-O bonds around 1400 cm^{-1} is presented in all nanocomposites, which appear at lower wavenumbers than typical carbonyl functional groups. This red shift confirmed the connection of oxygens atoms of linkers to Ti. Peaks around 470–480 cm^{-1} are related to Ti–O bonds, revealing that conjugation of MOF and polymer did not lead to degradation of the MOFs' structure (Fig. 1B). All other synthesized materials' FT-IR spectra are investigated in supplementary (Figs. S1 and S2).

The DLS and zeta potential of prepared compounds are shown in Figs. 1C and D, and S12–S19. For instance, the particle size (Z-Average (r.nm)) of NH_2-MIL-125(Ti) was about 41% more than MIL-125(Ti) and it would be due to more hydrogen bonding. It is noticeable that we reported the size of not-filtered samples because optimization of size and zeta potential were not the aim of the current study. The zeta potential of C2 was 3.4 times more than C1 (10.6, 2.41 mV respectively). Based on the zeta potential data, the MILs' surface charge is negative, and the C1 and C2 have a positive charge that leads to a better connection between MILs and Cs. In the case of composites, the amalgamation of Cs with MIL-125(Ti) led to different size distributions. The addition of C1 to MIL-125(Ti) which has lower $\Delta\zeta$ led to a decrease in the size of the final composite (MIL-125(Ti)@C1) compared to MIL-125(Ti), and the addition of C2 which has higher $\Delta\zeta$ led to size enlargement. The amalgamation of Cs with NH_2-MIL-125(Ti) led to a decrease in the final composite size compared to NH_2-MIL-125(Ti). As a scientific fact, the composition is a reliable method for changing the particle size and zeta potential of the final compound. For instance, the zeta potential of MIL-125(Ti)@C2 in comparison with other composites is more positive and confirms that by changing and optimizing the ratio of MILs and Cs, a desirable surface charge can be obtainable. The BET surface area of MIL-125 (Ti) after functionalization with amine groups has been decreased about 33.5%, BJH Adsorption cumulative volume of pores (17–3000 Å diameter) decreased approximately 41.0%, and BJH Adsorption average pore diameter (4 V/A) dwindled near 42.8% which decreasing these criteria amount has been reported severally and are in good agreement with literature (Figs. 1E and S20–S21). As a matter of example, Kim et al. reported that functionalization of MIL-125 (Ti) with amine groups led to

approximately 40 $m^2.g^{-1}$ reduction in BET surface area which is due to the occupation of the pores with amine groups [58, 59].

The surface morphology of prepared compounds is observed by scanning microscopy (Fig. 2). Comparing the MILs' and Cs' FESEM images (Fig. S6) with final compounds' FESEM images revealed that the addition of C1 and C2 led to well-structured circular shapes for both MOFs specially NH_2-MIL-125(Ti) due to more hydrogen bonding. The irregulated and agglomerated morphology has not been seen in final compounds specifically in compounds consisting of the NH_2-MIL-125(Ti). The C1 and C2 partially covered the surface of MIL-125(Ti). It is noticeable that it tried to find the biggest particles due to better imaging. In another study, Lin et al. synthesized MIL-125 and NH_2-MIL-125; their FESEM micrographs showed similar results, but their nanocomposites have a larger size than this study's nanocomposites. They reported that after coating MOFs with chitosan and Pluronic F127, round cake-like crystals with higher structural regularity and lower size than pure MOFs resulted in [60, 61]. The mapping large-scale (10 μm) images are also added to the Fig. 2 for better visualization. Other synthesized compounds' FESEM images are reported in supplementary (Figs. S5 and S6).

The EDS and mapping of fabricated composites are demonstrated in Fig. 3. Based on the screened results, all elements (C, Ti, O, N, Fe, and Mn) are well distributed and the elements' mass percentages were in good agreement with reagents proportion. Other materials EDS and mapping are reported in supplementary (Figs. S3, S4, and S7).

High-resolution transmission electron microscopy (HRTEM) analyses confirm the integration of manganese ferrite nanoparticles within the polymer matrices in the nanocomposite samples. The images illustrate aggregated nanoparticles embedded throughout the semicrystalline polymeric structures, indicating interactions between the nanoparticle surfaces and the matrices. High-resolution imaging of sample C1 specifically exhibits lattice fringes corresponding to the (311) and (400) planes of $MnFe_2O_4$, with d-spacings of approximately 0.25 and 0.21 nm, respectively (digital micrograph software was used to estimate lattice spacing of the $MnFe_2O_4$ nanoparticles). These spacing measurements match x-ray diffraction data, verifying the cubic spinel configuration of the manganese iron oxide. Additional diffraction rings in the images index several planes of $MnFe_2O_4$, further supporting its crystalline characteristics. Morphological evaluations demonstrate spherical shapes and homogeneous ~500 nm diameters for the final synthesized nanocomposites, with uniform depositions of compounds C1 and C2 onto the metal–organic framework surfaces [62, 63] (Figs. 4 and S22).
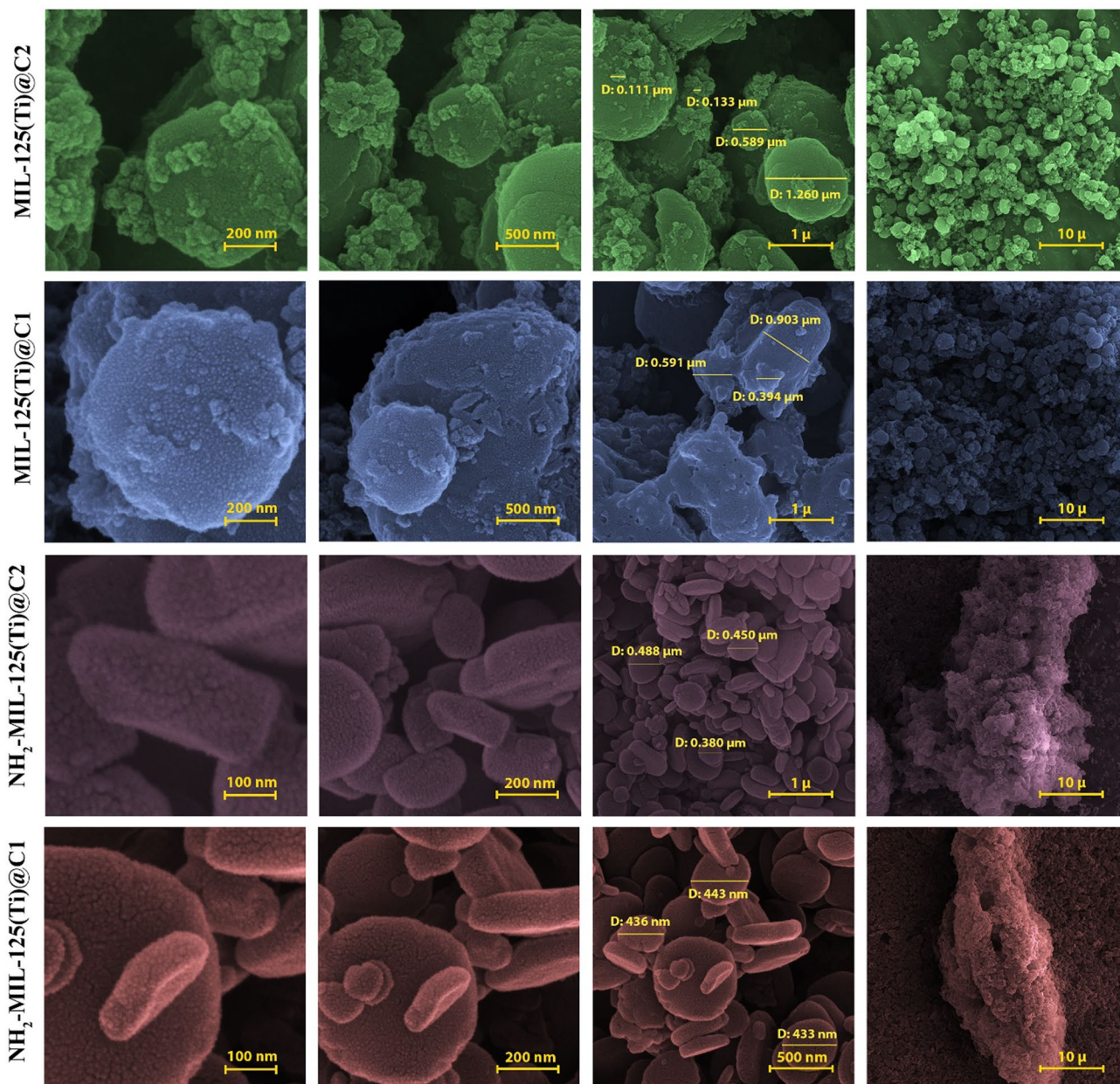
Fig. 2 The FESEM images of fabricated final compounds. MIL-125(Ti)@C2, MIL-125(Ti)@C1, NH$_2$-MIL-125(Ti)@C2, and NH$_2$-MIL-125(Ti)@C1. The scale bars and particle size are measured by Digimizer software

3.2 Drug loading and cellular uptake

Drug-loading efficiency of prepared compounds were as follows: MIL-125(Ti)@C1: 41.2%, MIL-125(Ti)@C2: 43.3%, NH$_2$-MIL-125(Ti)@C1: 70.7%, and NH$_2$-MIL-125(Ti)@C2: 75.4%. Mengru et al. report that changing the substituents of the linker can lead to different loading efficiency of ORI on MOF-5(Zn). Based on their study, the NH$_2$ substituent on BDC (terephthalic acid) led to a decrease in the loading efficiency compared to pristine BDC [64]. The higher loading efficiency of NH$_2$-MIL-125(Ti) in the current

study can be attributed to the different nature of the drug (DOX), metal node (Ti), and the presence of C1 and C2. The membrane structure, population, size, and altered and normal morphology of cells can be identified by comparing the cellular images with the literature [65, 66]. Comparing the cells' images after treatment by inorganic/organic hybrid compounds with literature demonstrates that utilizing these kinds of materials led to a negligible change in most cases in cell morphology [65]. Sun et al. reported that the cell membrane integrity was vastly destroyed after treatment with an inorganic compound [67]. The DOX delivery
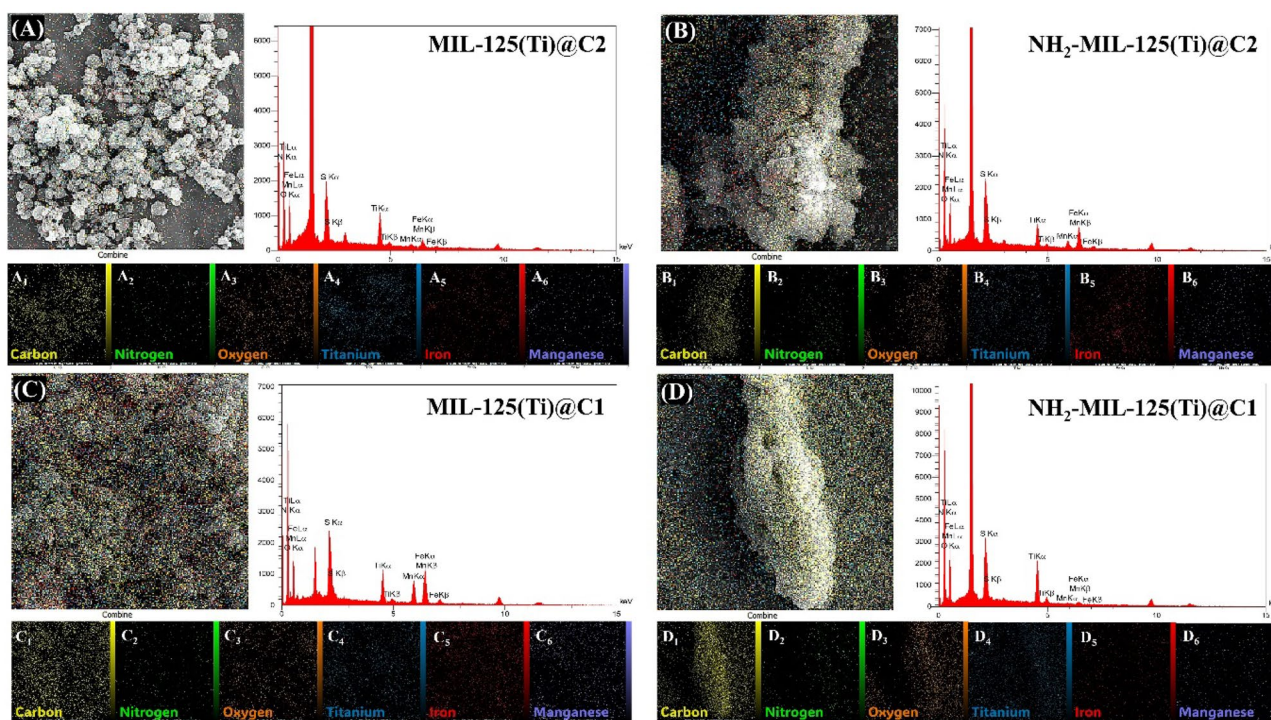
Fig. 3 The EDS and mapping of fabricated final compounds. **A** MIL-125(Ti)@C2, **B** NH$_2$-MIL-125(Ti)@C2, **C** MIL-125(Ti)@C1, and **D** NH$_2$-MIL-125(Ti)@C1

ability of prepared compounds is investigated after 4 h of treatment by CLSM and 2D fluorescence microscopy and the best results are reported. The CLSM images of treatments of the MIL-125(Ti)-based compounds on MCF-7 cells are shown in Fig. 5. The microscopic images demonstrate that treatment of MCF-7 cells with MIL-125(Ti)@ C1 has led to higher cell death compared to MIL-125(Ti)@ C2 that is in good agreement with cytotoxicity assessment results. Screening red-filter images disclosed that the MIL-125(Ti)-based compounds did not show reliable delivering ability in 2D fluorescence image compared to NH$_2$-MIL-125(Ti)-based compounds (Fig. 5C, D) so we tried changing the imaging instrument and staining material to achieve better results and the best results (their CLSM images) are reported (Fig. 5A, B). The cell population after treatment of MCF-7 cells with NH$_2$-MIL-125(Ti)-based compounds was much higher than MIL-125(Ti)-based compounds. The images of 2D fluorescence results of treated MCF-7 cells by NH$_2$-MIL-125(Ti)-based compounds reveal a higher cell population for NH$_2$-MIL-125(Ti)@C2 compared to NH$_2$-MIL-125(Ti)@C1 and also the DOX-related images of NH$_2$-MIL-125(Ti)@C2 are sharper than other compounds that could be owing to the presence of more

DOX in the cytoplasm. Although the cell population and sharpness of NH$_2$-MIL-125(Ti)-based compounds were better than MIL-125(Ti)-based compounds, these criteria were not good enough [68].

To increase the interactions and internalization of the cells, the cell-imprinted technique is utilized [69]. Dadashkhan and her colleagues developed the cell-imprinted substrate for inducing the P75 and S100 gene expression. They found that utilizing imprinted substrate can mimic the topography and morphology of cells which can lead to differentiation signal induction [54]. Also, in this method, the plate with optimized morphology for special cell culture theoretically leads to more efficient cellular interaction and internalization. Screening the images disclosed that the cell population considerably increased by applying the cell-imprinted substrate for the NH$_2$-MIL-125-based compounds. The sharpness of cell-nucleus dye is significantly higher than before and also comparing the DOX images showed that the internalization of DOX after cell imprinting considerably ran high and kept the morphology of cells, intact (Figs. 6 and 7). Although the loading efficiency of NH$_2$-MIL-125(Ti)@ C2 was higher than NH$_2$-MIL-125(Ti)@C1, it seems that the cell internalization and release of NH$_2$-MIL-125(Ti)@
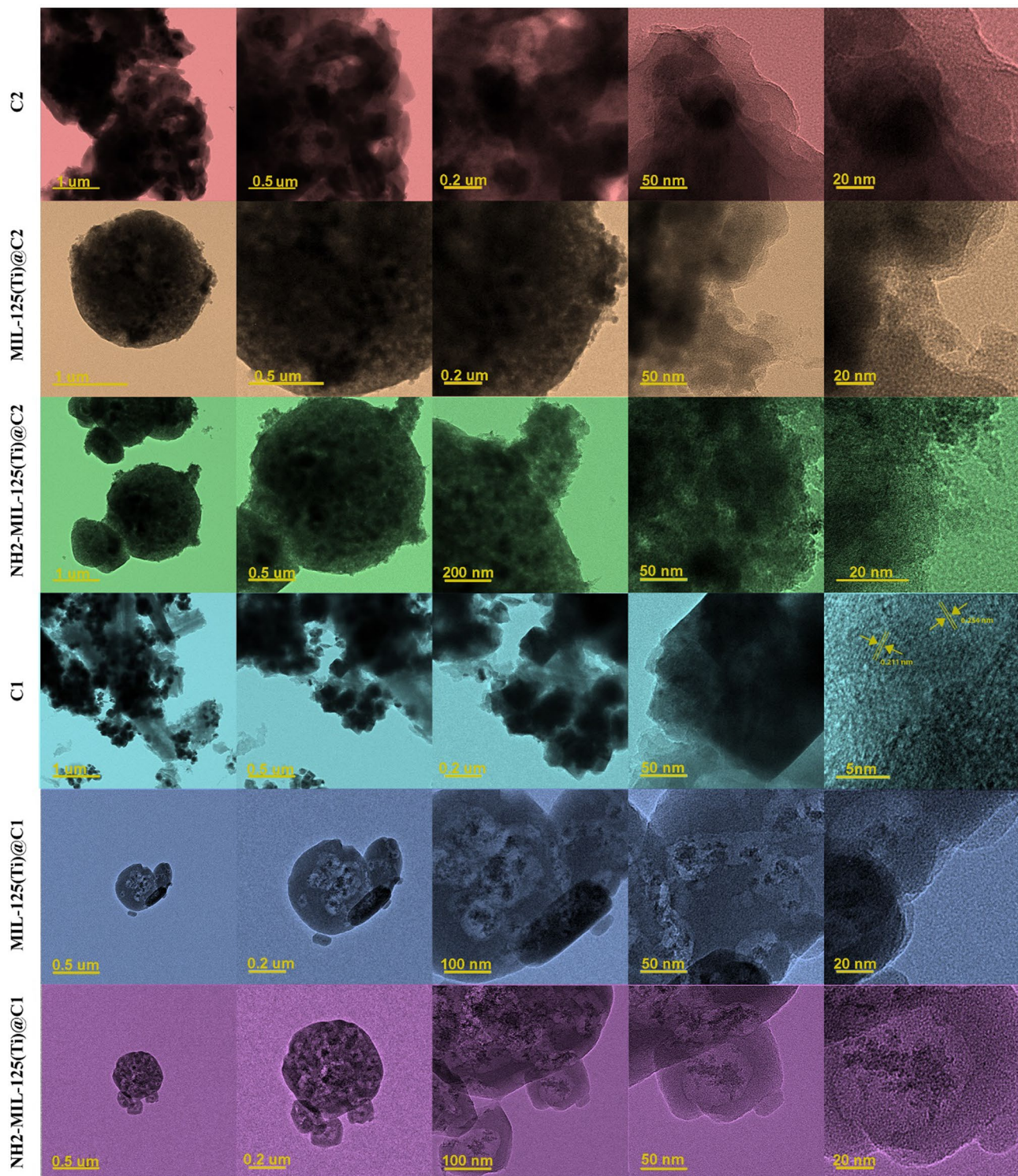
Fig. 4 The HRTEM images of C2, MIL-125(Ti)@C2, NH$_2$-MIL-125(Ti)@C2, C1, MIL-125(Ti)@C1, and NH$_2$-MIL-125(Ti)@C1

C1 is better than NH$_2$-MIL-125(Ti)@C2 due to higher DOX intensity. Based on the other reports, the interaction type can lead to changing the generation of ROS (reactive oxygen species) and can decrease or increase cytotoxicity [70].

3.3 The MTT assay

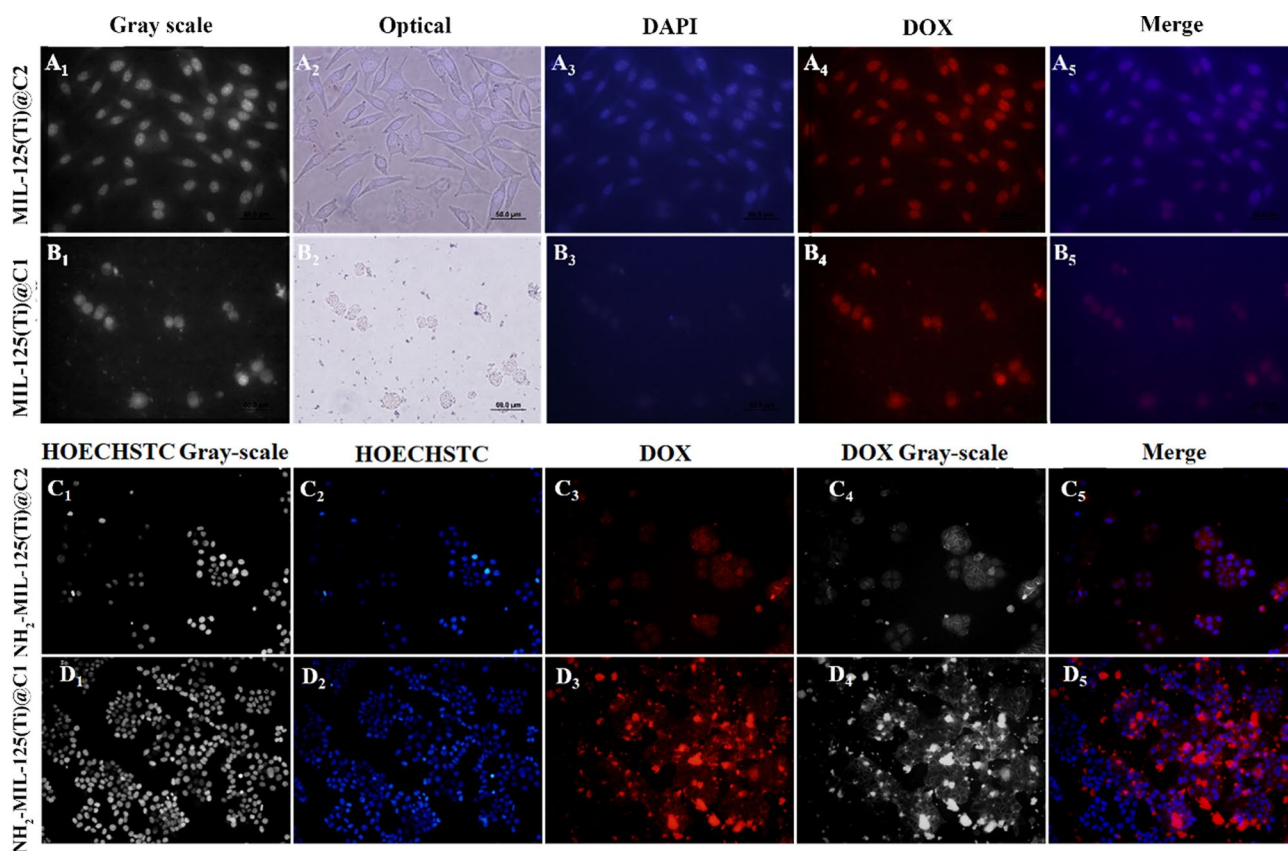High biocompatibility against healthy cells is requisite for any compounds with the purpose of gene/drug delivery.

Fig. 5 The 2D fluorescence images of **A** MIL-125(Ti)@C2, **B** MIL-125(Ti)@C1, **C** NH$_2$-MIL-125(Ti)@C1, and **D** NH$_2$-MIL-125(Ti)@C2

On the other hand, high anticancer activity is vital for cancer therapy. Although C1 and C2 revealed acceptable biomedical activity, some demerits should be addressed like low biological stability. Ashrafizadeh et al. investigated the cytotoxicity of PDA regarding substituents' position on four various cell lines (HEK-293, PC-12, MCF-7, and HT-29). Their results revealed that the highest cell viability among ortho, meta, and para substituents was related to para position [52]. Seydi and his colleagues have reported that although *p*PDA is widely used in the cosmetic industry, it has considerable toxicity and can enhance ROS generation, lipid peroxidation, and the collapse of mitochondrial membranes [71, 72]. Based on recent publications, utilizing the MIL-125(Ti) can lead to reliable biological stability, bioactivity, and biocompatibility due to the high LD50 value of the metal node (Ti) and linker (BDC) [30]. Luo and his colleagues have screened the cytotoxicity of NH$_2$-MIL-125(Ti) on NIH3T3, and based on their results, the cell viability of the mentioned compound was more than 90% [73]. In the other study, Khan et al. investigated the dose-dependent cytotoxicity of NH$_2$-MIL-125(Ti) in the three-time interval on the HepG2 cell line and their results disclose that the cytotoxicity of various dosages of NH$_2$-MIL-125(Ti) was under 10% [74]. So, the MIL-125(Ti) and NH$_2$-MIL-125(Ti) have been employed as a carrier of C1 and C2 to assess the surface amination effect as reported which leads to altered cytotoxicity and uptake [75]. In the present study, the cytotoxicity of prepared compounds was investigated by various cell lines, MCF-7, NIH3T3, and HEK-293 in 24- and 48-h time intervals (Fig. 8). The cell viability of MIL-125(Ti) (cell viability: 66–87% after 24-h treatment) was lower than NH$_2$-MIL-125(Ti) (67–90%) in all three cell lines. The cell viability of C2 (73–86%) was more than C1 (67–84%) due to the addition of aniline to the composite structure. The cytotoxicity of all compounds led to a lower cell population after 48 h compared to 24 h and the abovementioned trends mostly repeated after 48 h. The lowest sensitivity to the prepared compounds is related to the NIH3T3 cell line (more than 80%) and the biocompatibility of all compounds was almost steady. The addition of MIL-125(Ti) to the C1 and C2 has led to decreasing the cytotoxicity (~8%) on the MCF-7 cell line and also utilizing the NH$_2$-MIL-125(Ti) has enhanced the cell viability (~9%) of final compounds in comparison with MIL-125(Ti)-based
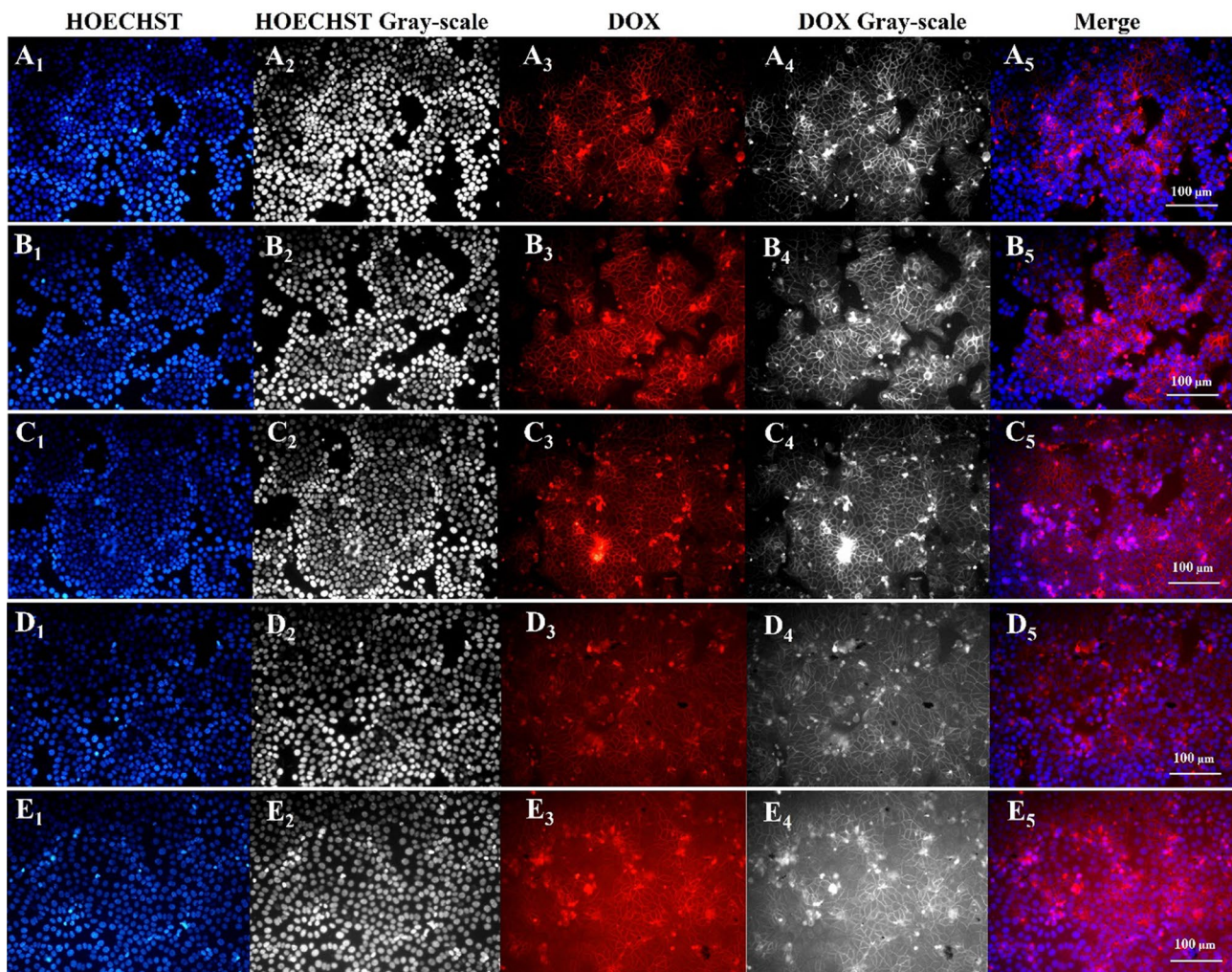
Fig. 6 2D fluorescence image results of cell-imprinted cell culture of NH$_2$-MIL-125(Ti)@C1

compounds. Based on these results, using the MIL-125(Ti) or NH$_2$-MIL-125(Ti) beside C1 and C2 has considerably enhanced the biocompatibility of C1 and C2. The heat map graphs in Fig. 8 disclose that all prepared compounds have dose-dependent behavior.

The hemolysis test is an important step in initially assessing how medications and chemicals that come in contact with blood might affect the body. This analysis is assumed valuable in pinpointing human health potential threats, such as kidney issues and hemolytic anemia. This relatively easy and simply conducted assay can provide precious insights into potential risks. The result of the hemolysis test after the treatment of prepared compounds and fabricated composites demonstrated that the hemolysis percentages for all the compounds were about one percent or less. In the case of MIL-125(Ti)-based composites, the lowest hemolysis percentage was related to was related to MIL-125(Ti)@C2, and in the case of NH$_2$-MIL-125(Ti), the NH$_2$-MIL-125(Ti)@C2 illustrated lower hemolysis percentage compared to NH$_2$-MIL-125(Ti)@C1 which are in good agreement with MTT assay results. As can be seen in Fig. 8M and N, the cytotoxicity of C1 was higher than C2, and every composite that C2 contained, demonstrated a lower hemolysis percentage. In one study, Han et al. assessed the hemolytic percentage of their compound which has been obtained from (NH$_2$)-MIL-125(Ti). Based on their results, their compound showed less than 5% hemolysis after treatment of 80 μg/mL on red blood cells. This result ensured that their compound can be safe for in vivo application and their in vivo assessment confirmed the biocompatibility of the Ti-based compound [76].
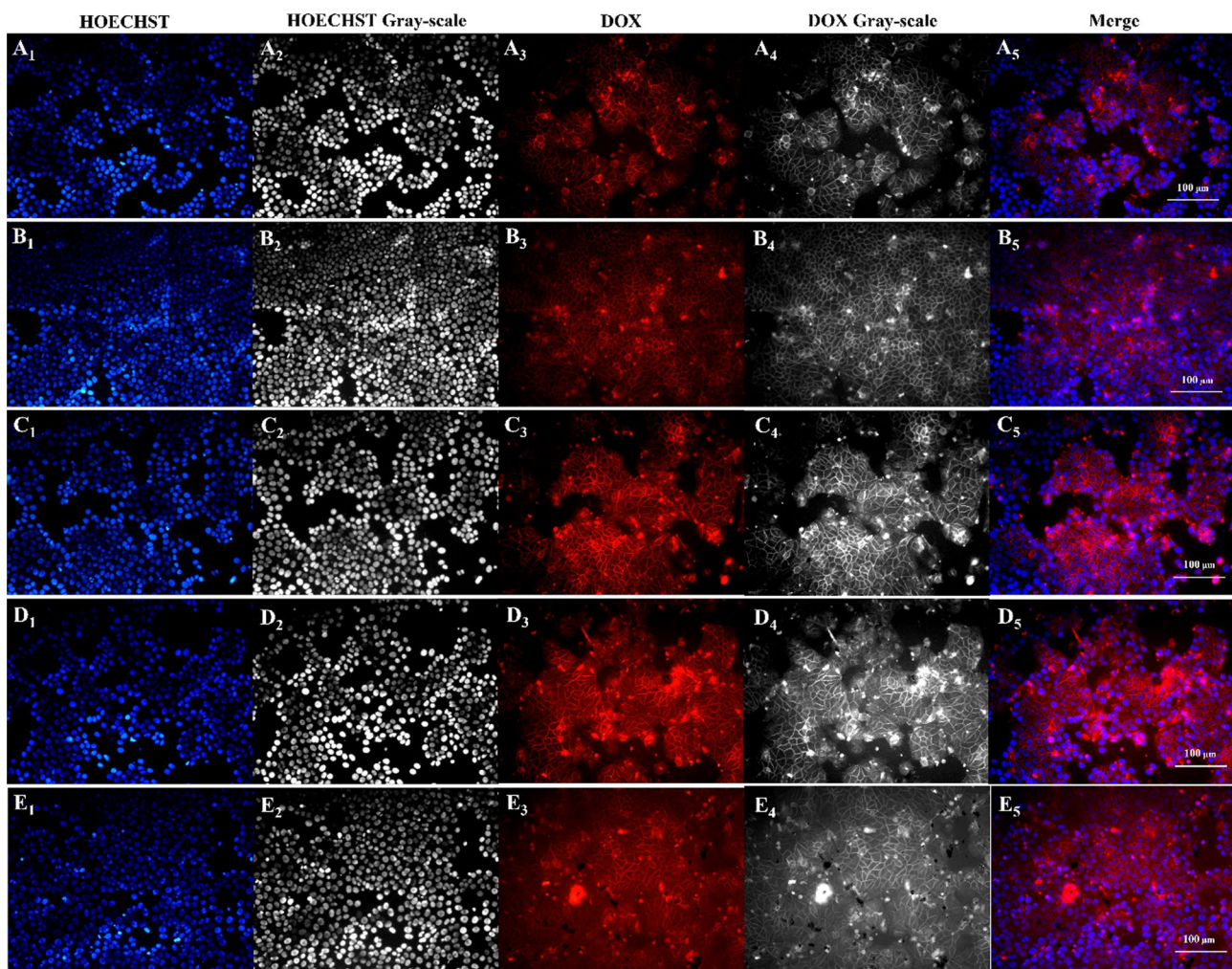
Fig. 7 2D fluorescence image results of cell-imprinted cell culture of NH_2-MIL-125(Ti)@C2

3.4 Gene delivery ability

The endosomal escape low performance, unacceptable absorbance of protons inside of ME (Microenvironment), poor transfection, and high cytotoxicity are the demerits of gene therapy methods. In this regard, the design and fabrication of compounds should be greener and can absorb protons of cellular ME. At our team's first attempt, the prepared nano-compound (coated UiO-66) only showed 6.4% transfection efficiency which impelled us to optimization of our vectors [13, 77]. The transfection ability of MOF-based nanocarriers is studied by Poddar et al. and they reported that their nano-compound has about 40% transfection efficiency [78]. In the current study, the gene transfection ability of final compounds as non-viral vectors is assessed (Fig. 9).

This study's results revealed that the gene (pCRISPR) transfection efficiency of prepared compounds to the A549 cell line was in the range of 16.6–38.3%. The lowest transfection was related to MIL-125(Ti)@C2: 16.6% and the highest was related to NH_2-MIL-125(Ti)@C1: 38.3%. Although the surface charge of the final compounds was not positive, it seems that the C1 and C2 with a positive
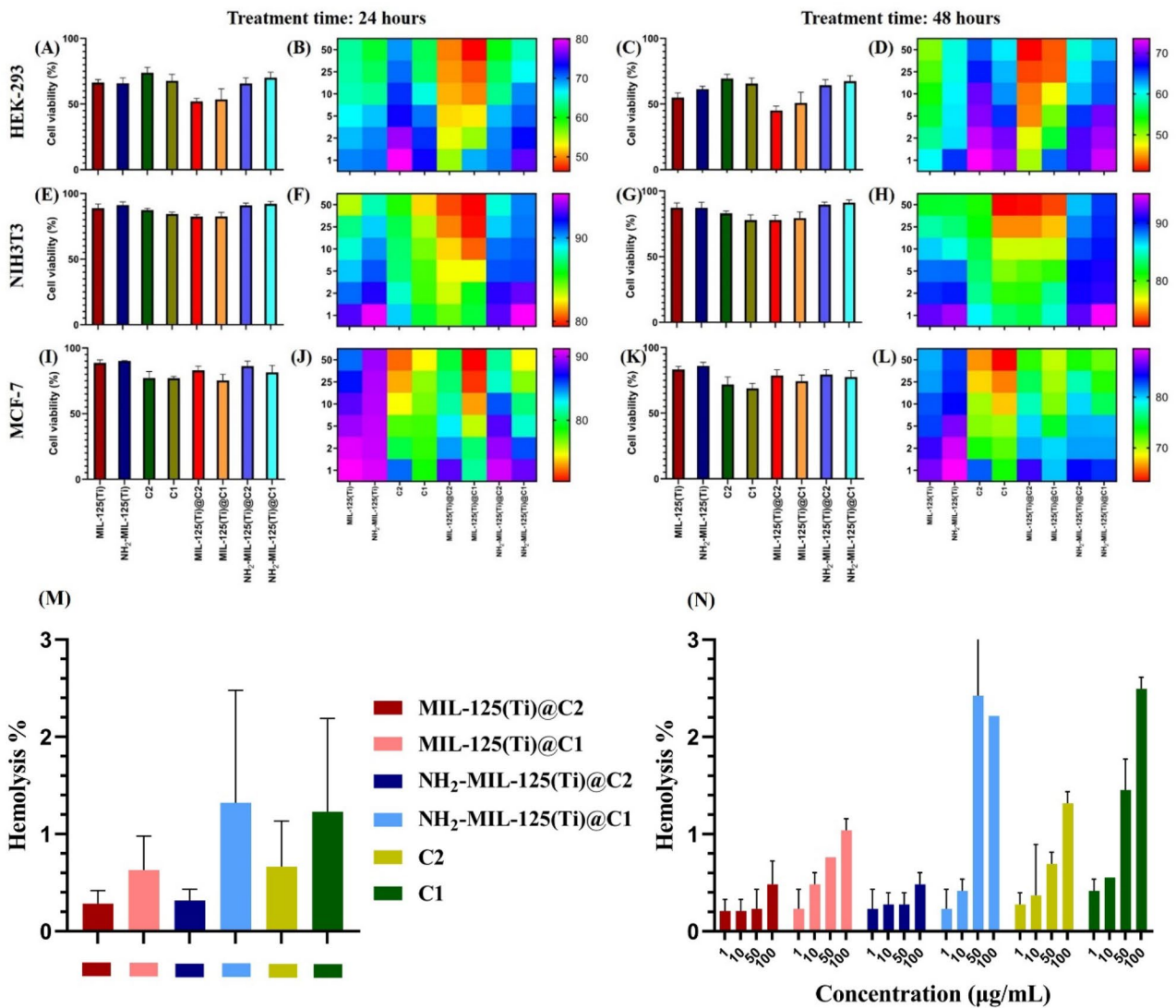
Fig. 8 The MTT assay on various cell lines (24 and 48 h treatment). **A** and **C** HEK-293, **E** and **G** NIH3T3, and **I** and **K** MCF-7. The heatmap graphs (dose-dependent behavior) of prepared compounds treated on **B** and **D** HEK-293, **F** and **H** NIH3T3, and **J** and **L** MCF-

7. The hemolysis analysis of prepared compounds and fabricated composites. **M** The median hemolysis percentages and **N** the dose-dependent (1, 10, 50, and 100 μg/mL) profile of hemolysis percentages

charge are responsible for gene transfection due to their positive zeta potential. Comparing the transfection efficiency of this study with published articles showed that more hydrogen bonding could be the reason for higher transfection efficiency for NH_2-MIL-125(Ti)-based compounds. The higher transfection ability of C1-contain compounds compared to C2-contain compounds can be

related to the lower cytotoxicity of these final compounds on HEK-293 and NIH-3T3 cell lines (Fig. 8) and better internalization of NH_2-MIL-125(Ti)@C1. These reported results demonstrate that fabricated compounds have the ability of efficient pCRISPR delivery to model cells. Some of the studies that have reported Gene/Drug co-delivery are listed in Table 1.
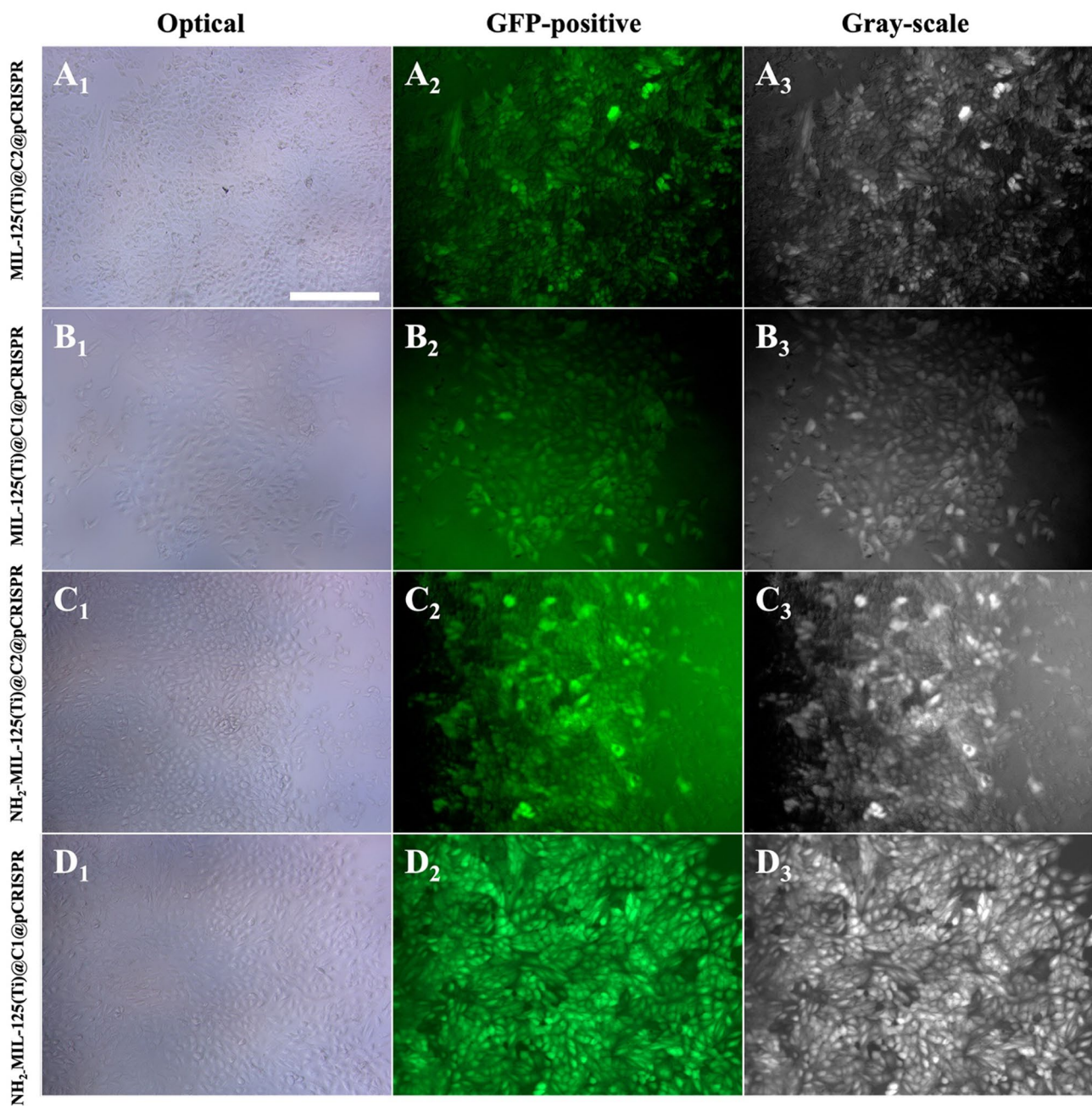
Fig. 9 The 2D fluorescence images of pCRISPR and GFP-loaded non-viral vectors transfected the A549 cell line. **A** MIL-125(Ti)@C2@pCRISPR, **B** MIL-125(Ti)@C1@pCRISPR, **C** NH$_2$-MIL-125(Ti)@C2@pCRISPR, and **D** NH$_2$-MIL-125(Ti)@C1@pCRISPR. The scale bar is 100 μm

Table 1 Some of the studies which have been assessed gene/drug co-delivery

Nanocomposite	Inorganic materials of the carrier	Drug	Genetic material	Modification	cell line	Types of therapy	Ref
CuS-RNP/@PEI	CuS	Doxorubicin	CRISPR-Cas9 ribonucleopro-tein (RNP)	PEI	MCF-7, A375	Photothermal, Chemotherapy, gene therapy	[79]
p(NIPAM)-GMA-UiO-66	GMA-UiO-66	Doxorubicin	pCRISPR	p(NIPAM)	HEK-293, HeLa, HepG2, PC12	Chemotherapy, gene therapy	[13]
SEHPA	Hollow mesoporous silica	Sorafenib	EpCAM-binding DNA aptamer, pEGFR	PAMAM	HepG2, Huh7	Chemotherapy, Gene Therapy	[80]
dCas9-MSN/ DOX/DNA	Mesoporous silica	Doxorubicin	CRISPR-dCas9	Tetrazine	HeLa	Chemotherapy, gene therapy	[81]
rGO/MWCNT/ ZnO/CoNi$_2$S$_4$/ alginate	rGO, MWCNT, ZnO	Doxorubicin	pCRISPR	Alginate, Leaf extract	HEK-293, HeLa, HepG2, PC12	Chemotherapy, Gene therapy	[82]
M-MSN/PEI-FA/ VEGF shRNA	Mesoporous silica, Fe$_3$O$_4$	Doxorubicin	VEGF shRNA	PEI, FA	HeLa, HUVEC	Gene therapy, chemotherapy	[83]
MXene/MOF-5/ chitosan	Ti$_3$C$_2$ MXene, MOF-5	Doxorubicin	pCRISPR	Chitosan	HEK-293, HeLa, HepG2, PC12	Gene therapy, chemotherapy	[23]
MXene/MOF-5/ alginate	Ti$_3$C$_2$ MXene, MOF-5	Doxorubicin	pCRISPR	Alginate	HEK-293, HeLa, HepG2, PC12	Gene therapy, chemotherapy	[23]
Bcl2-AuNPs	Gold nanoparticles	Doxorubicin	Bcl2-siRNA	3′-end thiolated siRNA	MDA-MB-231, MCF-7	Chemotherapy, gene therapy, wound healing	[84]
(GaN)$_{1-x}$(ZnO)$_x$/ chitosan	(GaN)$_{1-x}$(ZnO)$_x$ nanoparticles	Doxorubicin	pCRISPR	Chitosan	HEK-293, HeLa, HepG2, PC12	Gene therapy, chemotherapy	[85]
Fe$_3$O$_4$/MWCNT-COOH/Extract/ PdL/Extract	Fe$_3$O$_4$, MWCNT-COOH, PdL	Doxorubicin	pCRISPR	Natural extract	HEK-293, MCF-7, PC-12	Gene therapy, chemotherapy	[68]

4 Conclusion

Gene therapy is a rapidly advancing field of medicine that seeks to cure or alleviate genetic disorders by delivering therapeutic nucleic acids to affected cells. One of the challenges in gene therapy is the efficient and safe delivery of therapeutic nucleic acids to target cells. Several delivery systems have been developed, including viral vectors, non-viral vectors, and physical methods like electroporation. In the current study, the MIL-125(Ti)-based composites were designed and fabricated, and then, amine-based modification was provided for enhancing the characteristics with the purpose of co-delivery of gene/drug delivery. The FESEM images disclosed that polymer-based nanocomposites (C1 and C2) were successfully loaded into and on the surface of MILs without considerable precipitation which made them utilizable in biomedical applications. The highest loading efficiency was about 75.4% which was related to NH$_2$-MIL-125(Ti)@C2. The 2D fluorescence image revealed the internalization ability of prepared compounds into the cells and cell-imprinted plate screening has shown sharper intensity and more cell population and the highest intensity was related to NH$_2$-MIL-125(Ti)@C1. The MTT assay of compounds demonstrated that aminated structures have higher cell viability on different cell lines. The gene (pCRISPR) transfection has been screened on the A549 cell line and the highest transfection efficiency was related to NH$_2$-MIL-125(Ti)@C1 with 38.3% transfection.

In the future, scientists can further investigate and optimize the MIL-125(Ti) conjugated different stimuli-responsive polymers anchored with a wide range of nanoparticles for gene delivery and expression. They can explore different modifications of the nanostructure to enhance their cellular uptake, transfection efficiency, and therapeutic efficacy. This can involve modifying the surface chemistry of the particles, varying the size and shape of the particles, or changing the composition of the particles. Researchers can also continue to investigate the use of different genome editing tools, such as TALENs and Zinc Finger Nucleases, in combination with the MIL-125(Ti) conjugated polymeric structures to compare their efficacy in gene delivery and cancer treatment. Moreover, they can explore the use of other therapeutics, such as small molecules or antibodies, in combination with the nanostructure to develop more effective cancer therapies. Additionally, researchers can investigate the use of advanced imaging and sensing techniques to better understand the

interactions between the nanostructure and cells. This can involve using techniques such as fluorescence imaging, electron microscopy, or biosensors to track the fate of the nanostructure in cells and monitor the expression of edited genes. Also, they can explore the use of personalized medicine approaches to tailor gene therapies to individual patients based on their genetic makeup and the specific characteristics of their cancer cells. This can involve using technologies such as CRISPR screening to identify genetic targets for therapy and developing personalized delivery systems that are optimized for individual patients.

The current study on enhancing gene delivery and expression in cancer cells using MIL-125(Ti) conjugated poly(aniline-co-para-phenylenediamine)@manganese ferrite-based nanostructures has several implications for environmental and health problems. Some of these implications include:

1. Reduced toxicity: traditional chemotherapy drugs can have severe side effects on healthy cells, leading to a range of symptoms such as nausea, fatigue, and hair loss. By using targeted gene therapies, it may be possible to reduce these side effects, leading to improved quality of life for cancer patients. In addition, reducing the toxicity of cancer treatments can also lead to improved environmental outcomes, as fewer toxic chemicals are released into the environment.

2. Increased specificity: targeted gene therapies can also minimize the off-target effects of cancer treatments, leading to more effective therapies with fewer side effects. For example, using the MIL-125(Ti) conjugated poly(aniline-co-para-phenylenediamine)@manganese ferrite-based nanostructure to deliver doxorubicin and pCRISPR to cancer cells may minimize the effects of the therapy on healthy cells, leading to improved treatment outcomes.

3. Reduced environmental impact: Traditional cancer treatments can have long-lasting impacts on the environment, as they can release toxic chemicals into water and soil systems. Using targeted gene therapies may reduce the number of chemicals released into the environment, leading to improved environmental outcomes.

4. Personalized medicine: the use of personalized gene therapies can improve patient outcomes by tailoring treatments to individual patients, rather than using a one-size-fits-all approach. This can lead to improved treatment efficacy, reduced healthcare costs, and improved patient satisfaction. For example, using CRISPR screening to identify genetic targets for therapy and developing personalized delivery systems that are optimized for individual patients may lead to improved patient outcomes and reduced healthcare costs over time.

CRISPR gene editing technology is a revolutionary tool with far-reaching implications for both the economy and health. The development of personalized gene therapies using CRISPR technology has the potential to transform the way we approach healthcare by improving treatment outcomes and reducing healthcare costs. Additionally, CRISPR-based diagnostic tools can provide earlier and more accurate disease detection, leading to better health outcomes and reduced healthcare expenditures. In the future, the continued advancement of CRISPR technology is expected to lead to the development of more targeted and effective treatments for a wide range of diseases, including cancer, genetic disorders, and infectious diseases. However, there are also important ethical and social considerations that must be taken into account as this technology continues to evolve. The successful implementation of CRISPR gene editing technology will require careful consideration of the potential risks and benefits, as well as an ongoing dialogue between researchers, policymakers, and the public to ensure that this technology is used responsibly and for the benefit of all.

Declarations

Competing interests The authors declare no competing interests.

References

1. Sun C-Y et al (2013) Metal-organic frameworks as potential drug delivery systems. Expert Opin Drug Deliv 10(1):89–101
2. Wang Y et al (2020) Metal-organic frameworks for stimuli-responsive drug delivery. Biomaterials 230:119619

3. Cai M et al (2020) Metal organic frameworks as drug targeting delivery vehicles in the treatment of cancer. Pharmaceutics 12(3):232

4. Osterrieth JW, Fairen-Jimenez D (2021) Metal–organic framework composites for theragnostics and drug delivery applications. Biotechnol J 16(2):2000005

5. Lei B et al (2018) Constructing redox-responsive metal–organic framework nanocarriers for anticancer drug delivery. ACS Appl Mater Interfaces 10(19):16698–16706

6. Cai W et al (2019) Metal–organic framework-based stimuli-responsive systems for drug delivery. Adv Sci 6(1):1801526

7. Maranescu B, Visa A (2022) Applications of metal-organic frameworks as drug delivery systems. Int J Mol Sci 23(8):4458

8. Lawson HD, Walton SP, Chan C (2021) Metal–organic frameworks for drug delivery: a design perspective. ACS Appl Mater Interfaces 13(6):7004–7020

9. Orellana-Tavra C, Mercado SA, Fairen-Jimenez D (2016) Endocytosis mechanism of nano metal-organic frameworks for drug delivery. Adv Healthcare Mater 5(17):2261–2270

10. Lu K et al (2018) Nanoscale metal–organic frameworks for therapeutic, imaging, and sensing applications. Adv Mater 30(37):1707634

11. Li S, Tan L, Meng X (2020) Nanoscale metal-organic frameworks: synthesis, biocompatibility, imaging applications, and thermal and dynamic therapy of tumors. Adv Func Mater 30(13):1908924

12. Singh N, Qutub S, Khashab NM (2021) Biocompatibility and biodegradability of metal organic frameworks for biomedical applications. J Mater Chem B 9(30):5925–5934

13. Rabiee N et al (2021) Polymer-coated NH2-UiO-66 for the codelivery of DOX/pCRISPR. ACS Appl Mater Interfaces 13(9):10796–10811

14. Fu D-Y et al (2022) Polymer-metal-organic framework hybrids for bioimaging and cancer therapy. Coord Chem Rev 456:214393

15. Christodoulou I et al (2021) Degradation mechanism of porous metal-organic frameworks by in situ atomic force microscopy. Nanomaterials 11(3):722

16. Zheng Q et al (2019) Metal–organic frameworks incorporated polycaprolactone film for enhanced corrosion resistance and biocompatibility of Mg alloy. ACS Sustain Chem Eng 7(21):18114–18124

17. He S et al (2021) Metal-organic frameworks for advanced drug delivery. Acta Pharm Sin B 11(8):2362–2395

18. Molavi H, Moghimi H, Taheri RA (2020) Zr-based MOFs with high drug loading for adsorption removal of anti-cancer drugs: a potential drug storage. Appl Organomet Chem 34(4):e5549

19. Osman DI et al (2019) Nucleic acids biosensors based on metal-organic framework (MOF): paving the way to clinical laboratory diagnosis. Biosens Bioelectron 141:111451

20. Bieniek A et al (2021) MOF materials as therapeutic agents, drug carriers, imaging agents and biosensors in cancer biomedicine: recent advances and perspectives. Prog Mater Sci 117:100743

21. Zhong M, Kong L, Li N, Liu Y-Y, Zhu J-H (2019) Synthesis of MOF-derived nanostructures and their applications as anodes in lithium and sodium ion batteries. Coord Chem Rev 388:172–201

22. Huang K et al (2022) A double-layer carbon nanotubes/polyvinyl alcohol hydrogel with high stretchability and compressibility for human motion detection. Eng Sci 17:319–327

23. Rabiee N et al (2021) Natural polymers decorated MOF-MXene nanocarriers for co-delivery of doxorubicin/pCRISPR. ACS Appl Bio Mater 4(6):5106–5121

24. Giliopoulos D, Zamboulis A, Giannakoudakis D, Bikiaris D, Triantafyllidis K (2020) Polymer/Metal Organic Framework (MOF) Nanocomposites for Biomedical Applications. Molecules 25:185

25. Kalaj M, Bentz SA Jr, Palomba JM, Barcus KS, Katayama Y, Cohen SM (2020) Chem Rev 120:8267–8302

26. Liu S et al (2014) Exploring and exploiting dynamic noncovalent chemistry for effective surface modification of nanoscale Metal–organic frameworks. ACS Appl Mater Interfaces 6(8):5404–5412

27. Kumari M et al (2021) Rapid analysis of trace sulphite ion using fluorescent carbon dots produced from single use plastic cups. Eng Sci 17:101–112

28. Márquez AG et al (2016) Biocompatible polymer–metal–organic framework composite patches for cutaneous administration of cosmetic molecules. J Mater Chem B 4(43):7031–7040

29. Vyas S et al (2021) High performance conducting nanocomposites polyaniline (PANI)-CuO with enhanced antimicrobial activity for biomedical applications. ES Mater Manuf 15:46–52

30. Rengaraj A et al (2017) Porous NH2-MIL-125 as an efficient nano-platform for drug delivery, imaging, and ROS therapy utilized low-intensity visible light exposure system. Colloids Surf B 160:1–10

31. Fan G et al (2016) Bio-inspired polymer envelopes around adenoviral vectors to reduce immunogenicity and improve in vivo kinetics. Acta Biomater 30:94–105

32. Kosaraju SL (2005) Colon targeted delivery systems: review of polysaccharides for encapsulation and delivery. Crit Rev Food Sci Nutr 45(4):251–258

33. Mu Q et al (2023) Supramolecular self-assembly synthesis of hemoglobin-like amorphous CoP@ N, P-doped carbon composites enable ultralong stable cycling under high-current density for lithium-ion battery anodes. Adv Compos Hybrid Mater 6(1):23

34. Battistella C, Klok HA (2017) Controlling and monitoring intracellular delivery of anticancer polymer nanomedicines. Macromol Biosci 17(10):1700022

35. Hu L et al (2022) Stimuli-responsive charge-reversal MOF@ polymer hybrid nanocomposites for enhanced co-delivery of chemotherapeutics towards combination therapy of multidrug-resistant cancer. J Colloid Interface Sci 608:1882–1893

36. Guo J et al (2023) Reversing the negative effect of adenosine A1 receptor-targeted immunometabolism modulation on melanoma by a co-delivery nanomedicine for self-activation of anti-PD-L1 DNAzyme. Nano Today 48:101722

37. Lu L et al (2020) Metal organic framework@ polysilsesquioxane core/shell-structured nanoplatform for drug delivery. Pharmaceutics 12(2):98

38. Shahabi S et al (2015) Enhancing cellular uptake and doxorubicin delivery of mesoporous silica nanoparticles via surface functionalization: effects of serum. ACS Appl Mater Interfaces 7(48):26880–26891

39. Gong X et al (2018) Amine-functionalized silica nanoparticles with drug and gene co-delivery for anti-angiogenesis therapy of breast cancer. J Nanosci Nanotechnol 18(4):2379–2386

40. Liu Y et al (2017) Magnetic drug delivery systems. Sci China Mater 60(6):471–486

41. Kalaiselvan CR et al (2022) Manganese ferrite (MnFe2O4) nanostructures for cancer theranostics. Coord Chem Rev 473:214809

42. Kalaiselvan CR, Thorat ND, Sahu NK (2021) Carboxylated PEG-functionalized MnFe2O4 nanocubes synthesized in a mixed solvent: morphology, magnetic properties, and biomedical applications. ACS Omega 6(8):5266–5275

43. Li F et al (2023) Energy-and cost-efficient salt-assisted synthesis of nitrogen-doped porous carbon matrix decorated with nickel nanoparticles for superior electromagnetic wave absorption. Adv Compos Hybrid Mater 6(4):133

44. Dobson J (2006) Magnetic nanoparticles for drug delivery. Drug Dev Res 67(1):55–60

45. Yang K et al (2021) Oxygen-evolving manganese ferrite nanovesicles for hypoxia-responsive drug delivery and enhanced cancer chemoimmunotherapy. Adv Func Mater 31(11):2008078

46. Li F et al (2023) Morphology controllable urchin-shaped bimetallic nickel-cobalt oxide/carbon composites with enhanced electromagnetic wave absorption performance. J Mater Sci Technol 148:250–259

47. Nha T et al (2021) Sensitive MnFe 2 O 4–Ag hybrid nanoparticles with photothermal and magnetothermal properties for hyperthermia applications. RSC Adv 11(48):30054–30068

48. Hemmat A et al (2023) Magnetophoretic intranasal drug-loaded magnetic nano-aggregates as a platform for drug delivery in status epilepticus. Pharm Nanotechnol

49. Sohail M et al (2017) Synthesis of highly crystalline NH2-MIL-125 (Ti) with S-shaped water isotherms for adsorption heat transformation. Cryst Growth Des 17(3):1208–1213

50. Fu Y et al (2021) Fabrication of visible-light-active MR/NH2-MIL-125 (Ti) homojunction with boosted photocatalytic performance. Chem Eng J 412:128722

51. Bagherzadeh M et al (2022) MIL-125-based nanocarrier decorated with Palladium complex for targeted drug delivery. Sci Rep 12(1):1–15

52. Ashrafizadeh M et al (2022) Photoactive polymers-decorated Cu-Al layered double hydroxide hexagonal architectures: a potential non-viral vector for photothermal therapy and co-delivery of DOX/pCRISPR. Chem Eng J 448:137747

53. Kavand H et al (2019) Cell-imprint surface modification by contact photolithography-based approaches: direct-cell photolithography and optical soft lithography using PDMS cell imprints. ACS Appl Mater Interfaces 11(11):10559–10566

54. Dadashkhan S et al (2021) P75 and S100 gene expression induced by cell-imprinted substrate and beta-carotene to nerve tissue engineering. J Appl Polym Sci 138(26):50624

55. Rabiee N et al (2022) Calcium-based nanomaterials and their interrelation with chitosan: optimization for pCRISPR delivery. J Nanostructure Chem 12(5):919–932

56. Cho W-S et al (2013) Predictive value of in vitro assays depends on the mechanism of toxicity of metal oxide nanoparticles. Part Fibre Toxicol 10(1):1–15

57. Zhao Y et al (2019) A highly efficient composite catalyst constructed from NH2-MIL-125 (Ti) and reduced graphene oxide for CO2 photoreduction. Front Chem 7:789

58. Kim S-N et al (2013) Adsorption/catalytic properties of MIL-125 and NH2-MIL-125. Catal Today 204:85–93

59. Sunder N et al (2022) Development of amine-functionalized metal-organic frameworks hollow fiber mixed matrix membranes for CO2 and CH4 separation: a review. Polymers 14(7):1408

60. Lin Y-S et al (2022) De novo synthesis of a MIL-125 (Ti) carrier for thermal-and pH-responsive drug release. Biomaterials Advances 140:213070

61. Kulkarni AN et al (2021) Chemical solution deposition of Sb2Se3 films to study their structural, morphological and optical properties. ES Mater Manuf 15:96–102

62. Kumar S, Baruah S, Puzari A (2020) Poly (p-phenylenediamine)-based nanocomposites with metal oxide nanoparticle for optoelectronic and magneto-optic application. Polym Bull 77:441–457

63. Monunith A, Rajan A, Sahu NK (2020) Comparative study of enzymatic and non-enzymatic detection of glucose using manganese ferrite nanoparticles. Mater Res Express 7(9):094001

64. Cai M et al (2020) Functionalization of MOF-5 with monosubstituents: effects on drug delivery behavior. RSC Adv 10(60): 36862–36872

65. Van Zijl C et al (2008) In vitro effects of 2-methoxyestradiol on MCF-12A and MCF-7 cell growth, morphology and mitotic spindle formation. Cell Biochem Funct 26(5):632–642

66. Hill SM, Blask DE (1988) Effects of the pineal hormone melatonin on the proliferation and morphological characteristics of human breast cancer cells (MCF-7) in culture. Can Res 48(21):6121–6126

67. Sun D et al (2015) Antibacterial activity of ruthenium (II) polypyridyl complex manipulated by membrane permeability and cell morphology. Bioorg Med Chem Lett 25(10):2068–2073

68. Bagherzadeh M et al (2022) Magnetic carbon–based nanocomposite decorated with palladium complex for co-delivery of DOX/pCRISPR. J Drug Deliv Sci Technol 78:103917

69. Bonakdar S et al (2016) Cell-imprinted substrates modulate differentiation, redifferentiation, and transdifferentiation. ACS Appl Mater Interfaces 8(22):13777–13784

70. Wydra RJ et al (2015) The role of ROS generation from magnetic nanoparticles in an alternating magnetic field on cytotoxicity. Acta Biomater 25:284–290

71. Seydi E et al (2019) The effects of para-phenylenediamine (PPD) on the skin fibroblast cells. Xenobiotica

72. Al-Harbi N et al (2021) Cellulose acetate-hydroxyapatite-bioglass-zirconia nanocomposite particles as potential biomaterial: synthesis, characterization, and biological properties for bone application. Eng Sci 17:70–82

73. Luo Y et al (2022) Simultaneously enhancing the photocatalytic and photothermal effect of NH2-MIL-125-GO-Pt ternary heterojunction for rapid therapy of bacteria-infected wounds. Bioact Mater 18:421–432

74. Khan ZA et al (2021) Selective antimicrobial and antibiofilm activity of metal–organic framework NH2-MIL-125 against Staphylococcus aureus. Mater Sci Eng B 269:115146

75. Hanot CC et al (2015) Effects of iron-oxide nanoparticle surface chemistry on uptake kinetics and cytotoxicity in CHO-K1 cells. Int J Mol Sci 17(1):54

76. Han X et al (2022) N-doping of the TiO2/C nanostructure derived from metal-organic frameworks with high drug loading for efficient sonodynamic & chemotherapy. Smart Mater Med 3:168–178

77. Safarkhani M, Saeb MR, Lee JH, Huh YS, Rabiee N (2023) Carbon-based nanomaterials for CRISPR/Cas delivery: a perspective on the design approach. Carbon Lett. https://doi.org/10.1007/s42823-023-00655-4

78. Poddar A et al (2019) Encapsulation, visualization and expression of genes with biomimetically mineralized zeolitic imidazolate framework-8 (ZIF-8). Small 15(36):1902268

79. Chen C et al (2021) Controlled CRISPR-Cas9 ribonucleoprotein delivery for sensitized photothermal therapy. Small 17(33):2101155

80. Zhang B-C et al (2020) Co-delivery of sorafenib and CRISPR/Cas9 based on targeted core–shell hollow mesoporous organosilica nanoparticles for synergistic HCC therapy. ACS Appl Mater Interfaces 12(51):57362–57372

81. Ma Y et al (2021) CRISPR-dCas9-guided and telomerase-responsive nanosystem for precise anti-cancer drug delivery. ACS Appl Mater Interfaces 13(7):7890–7896

82. Rabiee N et al (2021) Turning toxic nanomaterials into a safe and bioactive nanocarrier for co-delivery of DOX/pCRISPR. ACS Appl Bio Mater 4(6):5336–5351

83. Li T et al (2016) Folate-functionalized magnetic-mesoporous silica nanoparticles for drug/gene codelivery to potentiate the antitumor efficacy. ACS Appl Mater Interfaces 8(22):13748–13758

84. Tunç CÜ, Aydin O (2022) Co-delivery of Bcl-2 siRNA and doxorubicin through gold nanoparticle-based delivery system for a combined cancer therapy approach. J Drug Deliv Sci Technol 74:103603

85. Bagherzadeh M et al (2021) Zn-rich (GaN) 1–x (ZnO) x: a biomedical friend? New J Chem 45(8):4077–4089

Authors and Affiliations

Moein Safarkhani[1,2] · Amirhossein Ojaghi[2] · Shefa Mirani Nezhad[3] · Hossein Daneshgar[2] · Ana Cláudia Paiva-Santos[4,5] · Fatemeh Radmanesh[6,7] · Mojtaba Bagherzadeh[2] · Ehsan Nazarzadeh Zare[3] · Navid Rabiee[8,9] · Pooyan Makvandi[10,11]

✉ Ehsan Nazarzadeh Zare
  ehsan.nazarzadehzare@gmail.com; e.nazarzadeh@du.ac.ir

✉ Navid Rabiee
  nrabiee94@gmail.com

✉ Pooyan Makvandi
  pooyanmakvandi@gmail.com

1 Department of Biological Sciences and Bioengineering, NanoBio High-Tech Materials Research Center, Inha University, Incheon 402-751, Republic of Korea

2 Department of Chemistry, Sharif University of Technology, Tehran, Iran

3 School of Chemistry, Damghan University, Damghan 36716-45667, Iran

4 Department of Pharmaceutical Technology, Faculty of Pharmacy of the University of Coimbra, University of Coimbra, Coimbra 3000-548, Portugal

5 REQUIMTE/LAQV, Group of Pharmaceutical Technology, Faculty of Pharmacy of the University of Coimbra, University of Coimbra, Coimbra 3000-548, Portugal

6 Uro-Oncology Research Center, Tehran University of Medical Sciences, Tehran, Iran

7 Department of Stem Cells and Developmental Biology, Cell Science Research Center, Royan Institute for Stem Cell Biology and Technology, ACECR, Tehran, Iran

8 School of Engineering, Macquarie University, Sydney, NSW 2109, Australia

9 Centre for Molecular Medicine and Innovative Therapeutics, Murdoch University, Perth, WA 6150, Australia

10 The Quzhou Affiliated Hospital of Wenzhou Medical University, Quzhou People's Hospital, Quzhou, Zhejiang 324000, China

11 Centre of Research Impact and Outcome, Chitkara University Institute of Engineering and Technology, Chitkara University, Rajpura, Punjab 140401, India